JOURNAL OF MATERIALS SCIENCE 36 (2001) 4611–4616

Non-equilibrium crystallization diagram for the $Co_{75.26-x}Fe_{4.74}(BSi)_{20+x}$ amorphous metal alloys

C. K. KIM*, H. KYUNG, C. S. YOON
Department of Materials Science and Engineering, Hanyang University, Seoul, 133-791, Korea
E-mail: ckkim@hanyang.ac.kr

A non-equilibrium crystallization diagram for Co sub-surface layers of the $Co_{75.26-x}Fe_{4.74}(BSi)_{20+x}$ amorphous alloy for $x > 1$ during magnetic field annealing is determined using Transmission Electron Microscopy (TEM). The diagram shows that, depending on the composition and temperature, the Co sub-layer exhibits five distinctively different microstructures when the metallic glass is heat treated below its bulk crystallization temperature. At high boron content, the structure is dominated by the FCC structure with a high degree of oxygen impurity faulting regardless of the annealing temperature. At low concentration, the Co sub-layer exhibits FCC or HCP structures, depending on the temperature. Also found was a two-phase region in which FCC and HCP Co co-existed. Such a diagram serves as a useful guide to obtaining the desired properties as the microstructure is closely linked to the magnetic properties of the material.

1. Introduction

One of the most publicized applications of the Co-rich magnetic amorphous alloys involves the anti-theft security systems installed in retail stores. Such systems utilize the non-linear magnetic properties of the Co-rich amorphous material to generate sharp voltage pulses detected by a pick-up coil. Although other ferromagnetic materials such as square permalloy [1] or "wasp-waisted" constricted Perminvar loop [2] can be used for the purpose, these materials have the disadvantages of low mechanical and magnetic stability that could severely degrade the permeability during manufacturing and service.

In order to fabricate metallic glass sensors, amorphous ribbons are heat treated under an external magnetic field to obtain a unique signature in the hysteresis loop. During annealing, it is observed that the material undergoes a substantial amount of both oxidation and crystallization to create distinctively different microstructures [3, 4].

When the amorphous ribbon is heat treated well below its bulk crystallization temperature, a complex oxide structure develops which depends on the total content of the metalloid elements (B, Si) and the ratio of B/Si. As illustrated in Fig. 1, when the total content of B and Si exceeds the critical composition, 21 at.%, the ribbon surface is covered with a continuous layer of borosilicate glass. If the B + Si is below 21 at.%, islands of CoO will form on the surface and the amorphous alloy will lose the pinned domain structure [5]. The metalloid content not only determines the surface oxide, but also affects the crystalline Co sub-layer that lies underneath the surface oxide when the metalloid content exceeds the critical amount [4].

Cobalt exists in two forms of closed packed structures: HCP (Hexagonal Close Packed) and FCC (Face Centered Cubic) with a minimal difference in structural energy although HCP is slightly more stable at room temperature [6]. It was found that the structure of crystallized Co sub-layer in the amorphous ribbon can change depending on the B + Si content and the annealing temperature when the amount of B + Si was above the critical concentration. Furthermore, the crystallized Co sub-layer was heavily faulted with the oxygen-diffusion faults, where the excess amount of oxygen is preferentially condensed onto the Co lattice to generate stacking fault-like defects [7]. The metalloid content and the annealing temperature also dictate the density of the oxygen faults.

The importance of the microstructure of the crystalline Co sub-layer is that the sub-layer determines the magnetic properties of the material. The annealing of the amorphous ribbon is in the magnetic field to induce anisotropy in the magnetic behavior of the material. Fig. 2 illustrates schematically the hysteresis loop after the magnetic field annealing. The field-induced anisotropy is measured by the offset in the hysteresis loop as shown in Fig. 2, and it is found that the field-induced anisotropy strongly correlates with the presence and amount of the oxygen faults and the type of crystalline Co structure. When the Co sub-layer was either FCC or HCP which was free of the oxygen fault, H_{offset} was nearly zero, rendering the material useless

*Author to whom all correspondence should be addressed.

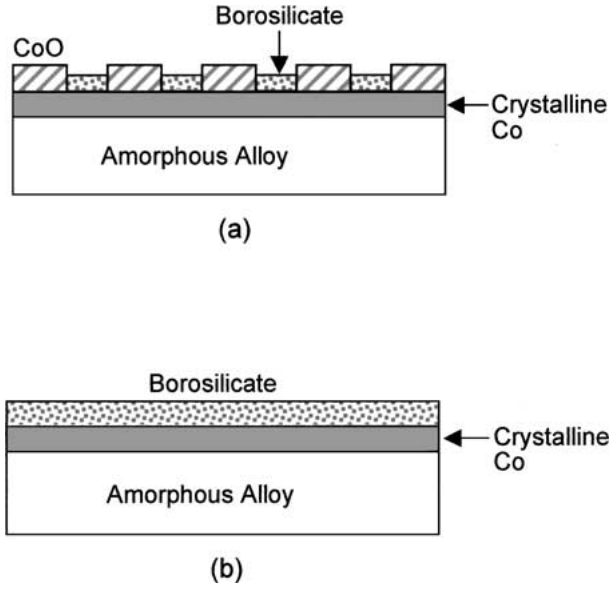

Figure 1 Schematic drawing of the microstructure of the amorphous $Co_{75.26-x}Fe_{4.74}(BSi)_{20+x}$ alloy after field annealing below the bulk crystallization temperature: (a) when the B + Si is below 21 at.%, (b) when the B + Si is above 21 at.%.

as a sensor while the largest H_{offset} was observed in the oxygen-faulted HCP structure [8].

Because the measure of the anisotropy ultimately determines the performance of the sensor material, it is of a great importance to map out the sub-layer microstructure as a function of the composition and temperature; thus, the Co microstructure of the amorphous alloy can be controlled to make a useful magnetic sensor. Since the amorphous alloy is in a meta-stable state, conventional phase diagrams do not apply. The structure at each data point has to be individually determined using analytical tools to produce a non-equilibrium crystallization diagram.

2. Experimental details

Various compositions of the amorphous $Co_{75.26-x}Fe_{4.74}(BSi)_{20+x}$ alloy were produced by planar flow casting at the Metglas Products Division of Allied-Signal Corporation. The following compositions were produced and annealed at different temperatures in the presence of a 60 Oe longitudinal magnetic field:

$Co_{74.26}Fe_{4.74}B_{21}$
$Co_{74.26}Fe_{4.74}B_{18.9}Si_{2.1}$
$Co_{70.5}Fe_{4.7}B_{15}Si_{10}$
$Co_{74.26}Fe_{4.74}B_{12.6}Si_{8.4}$
$Co_{74.26}Fe_{4.74}B_{8.4}Si_{12.6}$

Typical samples produced were 20 μm thick and 3 mm wide. Composition of the samples was verified by chemical analysis with X-ray photoelectron spectroscopy (XPS) and energy dispersive spectroscopy (EDS).

Differential scanning calorimetry(DSC) was used to determine the crystallization temperature. DSC (heating rate at 10°/min) indicates that the onset of the crystallization of amorphous $Co_{75.26-x}Fe_{4.74}(BSi)_{20+x}$ occurs at 465°C with its maximum peak at 535°C.

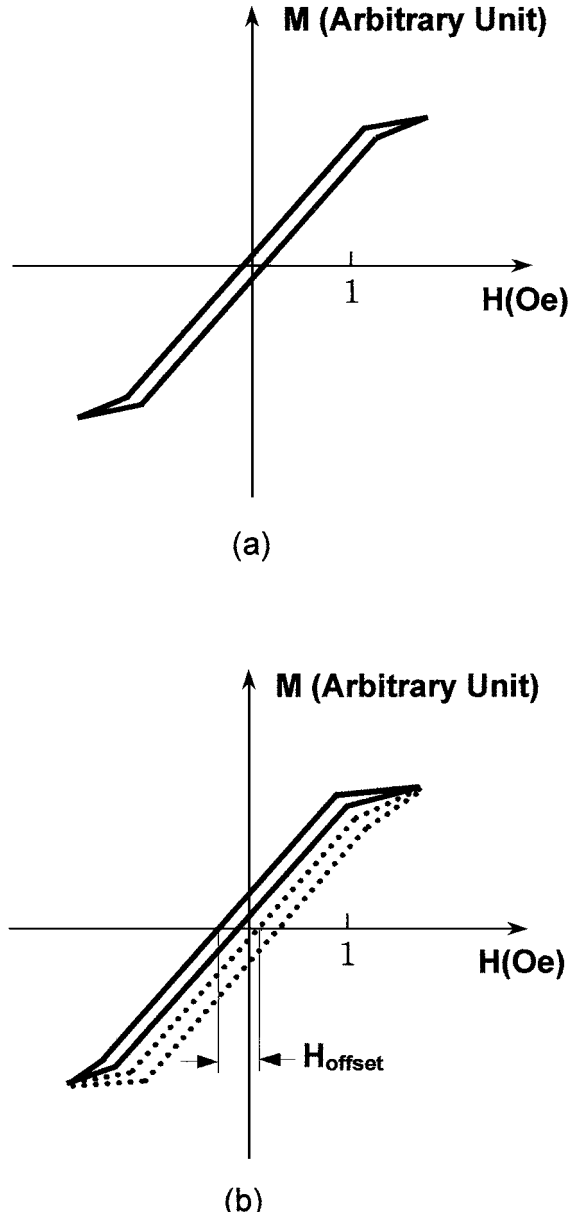

Figure 2 Schematic drawing of M-H loops for Co-rich amorphous alloy. (a) After field annealing and a.c. demagnetization (b) After positive (solid line) and negative (dotted line) field pulses of order 200 Oe. The field-induced anisotropy is estimated by H_{offset}.

Therefore, the annealing of the samples was done at 200°C–450°C below the measured crystallization temperature.

Traditionally, the investigation of crystallization of amorphous material has been based upon macroscopic techniques such as differential scanning calorimetry and X-ray scattering [9–11]. Such macroscopic characterization tools often provide misleading information due to averaging effects and $Co_{75.26-x}Fe_{4.74}(BSi)_{20+x}$ is especially difficult to analyze using macroscopic means due to its complex oxidation behavior involving multi-phases. Here, we have employed the Transmission Electron Microscopy (TEM, JEOL 200CX and EM-002B) to obtain direct microstructural evidence of the Co sub-layer during early stages of field annealing. The TEM samples were prepared using an ion mill equipped with a liquid-nitrogen cooled cold stage to ensure minimal heating of the sample during milling.

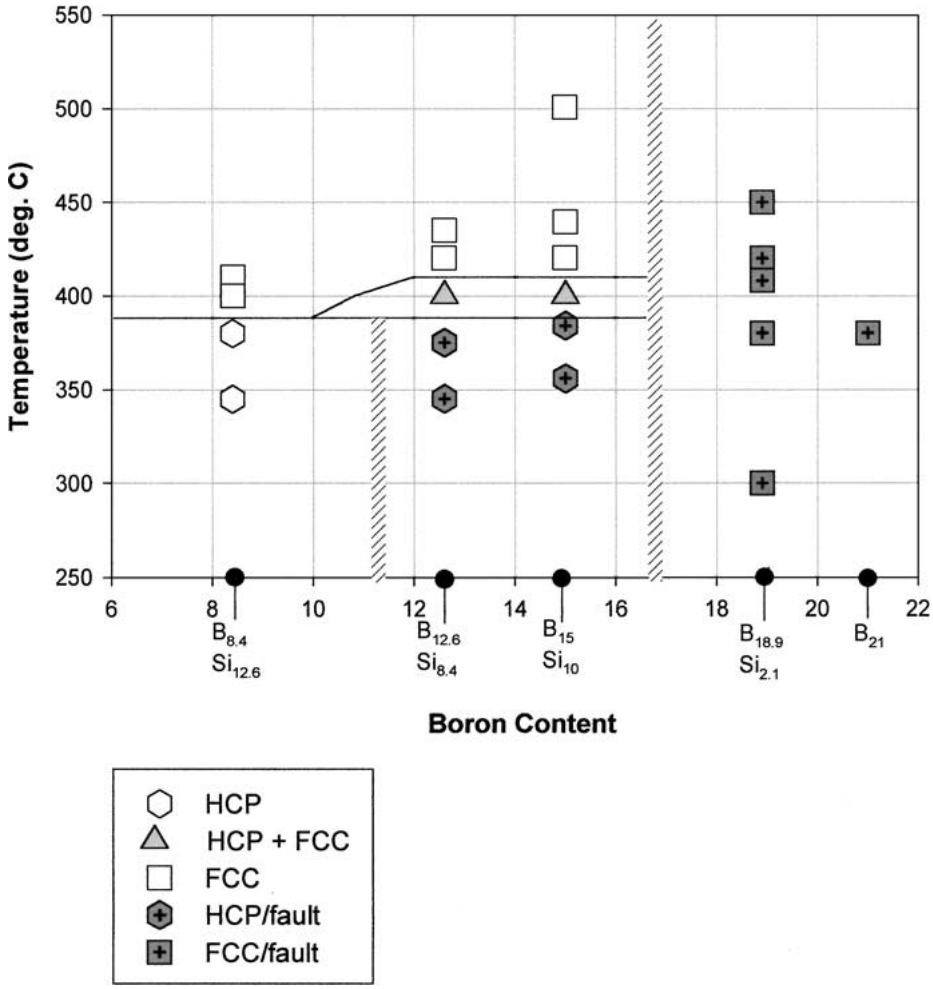

Figure 3 Non-equilibrium crystallization diagram for the amorphous $Co_{75.26-x}Fe_{4.74}(BSi)_{20+x}$ alloy.

3. Results and discussion

Fig. 3 shows the non-equilibrium crystallization diagram for $Co_{75.26-x}Fe_{4.74}(BSi)_{20+x}$ amorphous alloy when the total content of B and Si was above 21 at.%. The non-equilibrium diagram is constructed using TEM to provide structural information on each data point. Five regions with distinctively different Co microstructures were found in the sub-layer. Fig. 4 shows TEM micrographs from each region.

As the boron content and the annealing temperature increased, the FCC structure tends to be stabilized. There is a boundary between 16 at.% and 18 at.% of boron above which a heavily faulted FCC structure was found in the Co sub-layer regardless of the annealing temperature. Shown in Fig. 4a is the faulted FCC Co, where abundance of fine lines inside the grains is indicative of the oxygen fault, which can be also inferred from the absence of (200) peak and existence of streaks in the electron diffraction pattern [7]. Below the "16–18 at.%" boundary, the sub-layer structure is divided around 400°C. Above 400°C, FCC structure without oxygen faults (Fig. 4b, notice the absence of fine lines inside the grains.) developed in the sub-layer while above 450°C, bulk crystallization occurred destroying the multi-layer surface structure. Below 400°C, HCP structure was found in the crystallized Co layer with the oxygen faults occurring at the boron-rich end of the HCP-stable region. Fig. 4c shows the Co grains with the oxygen fault developing within the amorphous matrix while Fig. 4d shows the grains with the HCP structure, free of the oxygen impurity faults. Also found in this region is the a two-phase region around 400°C at the boron-rich end of the HCP-stable region. Shown in Fig. 4e is the micrograph of the fault-free HCP and faulted FCC phases existing together in the Co sub-layer.

In general, the increased content of boron appears to promote the formation of the oxygen fault. This tendency can be explained by the difference in the amorphous structure of the B_2O_3-rich and the SiO_2-rich phases. As the B/Si ratio increases, the surface oxide is dominated by the B_2O_3-rich phase. An electron diffraction study of the B_2O_3-rich and SiO_2-rich oxides showed that the B_2O_3-rich phase exhibited weak atomic correlations, i.e. disordered and porous structure compared with the SiO_2-rich oxide [12]. The porous nature of the B_2O_3-rich surface oxide would allow a larger amount of oxygen to be supplied to the subsurface layer. The inflow of the oxygen stabilized the high temperature form of Co (FCC) during the field-annealing and condensed on FCC {111} planes regardless of the annealing temperature. In the case of Si-rich end of the diagram, the dense SiO_2-rich surface oxide retards the diffusion of oxygen into the subsurface layer, leading to the formation of fault-free HCP and FCC structures, depending on the annealing temperature.

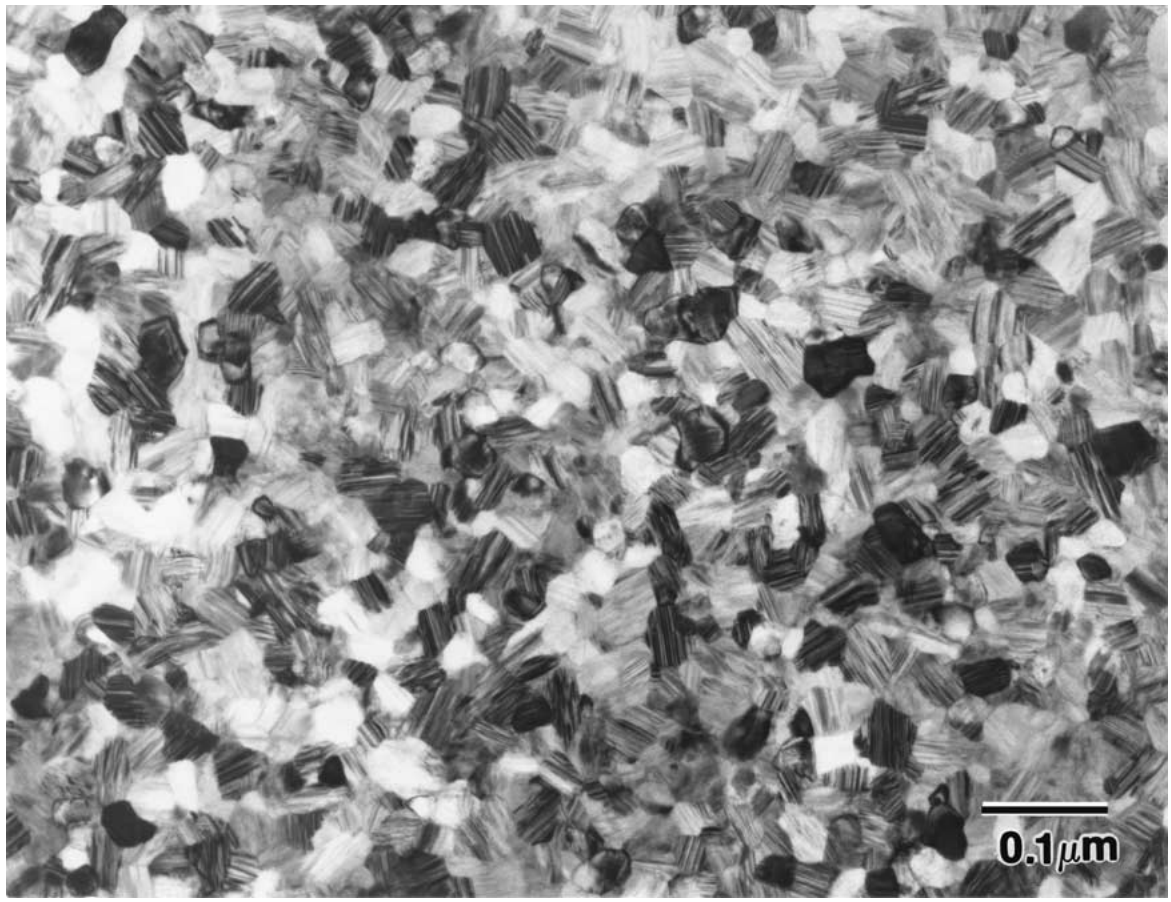

(a)

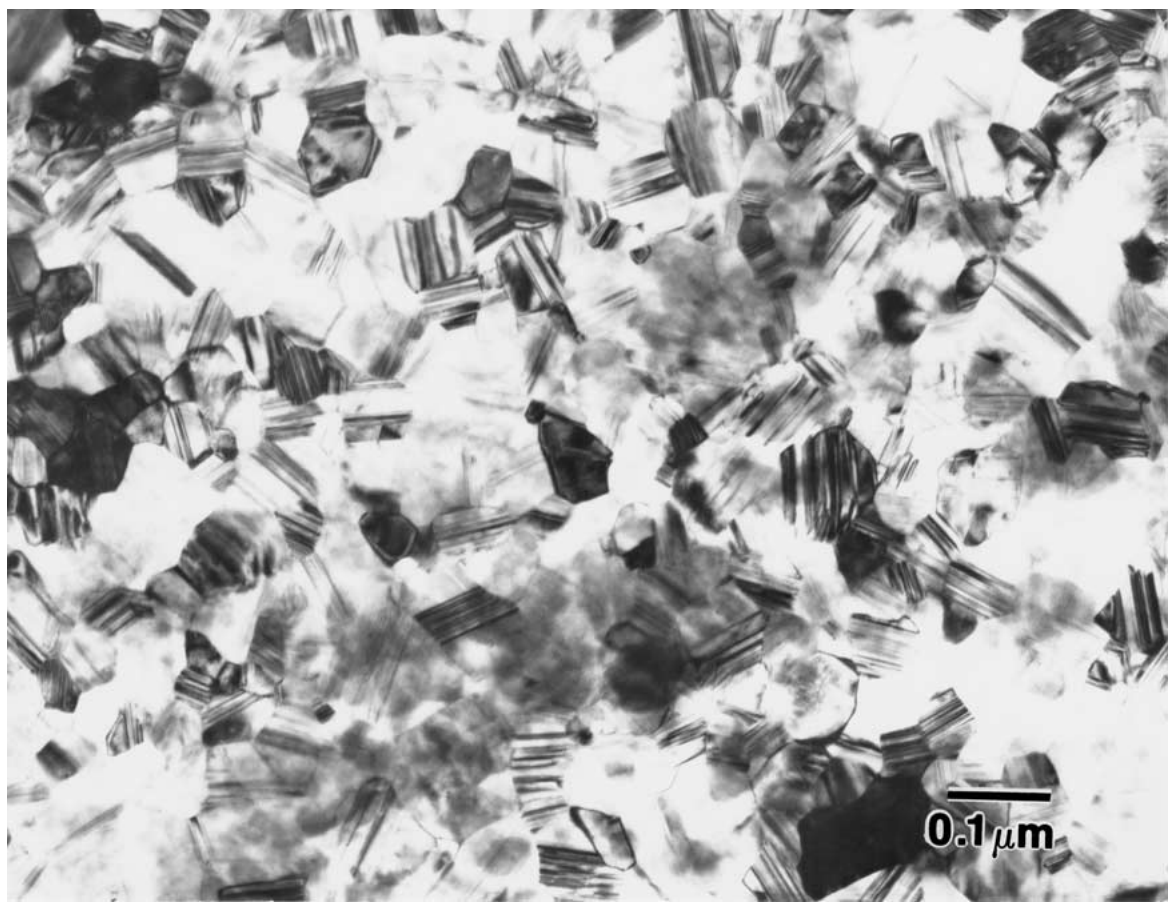

(b)

Figure 4 Bright field TEM micrographs of each microstructure representing the different phase regions in the crystallization diagram of Fig. 3. (a) $Co_{74.26}Fe_{4.74}B_{18.9}Si_{2.1}$ annealed at 408°C for 19 min. showing faulted FCC, (b) $Co_{70.5}Fe_{4.7}B_{15}Si_{10}$ annealed at 440°C for 30 min. showing FCC without faults, (c) $Co_{70.5}Fe_{4.7}B_{15}Si_{10}$ annealed at 356°C for 30 min. showing faulted HCP grains, (d) $Co_{74.26}Fe_{4.74}B_{8.4}Si_{12.6}$ annealed at 380°C for 60 min. showing HCP without faults, (e) $Co_{74.26}Fe_{4.74}B_{12.6}Si_{8.4}$ annealed at 400°C for 30 min. showing two phases (HCP and FCC) with the phase boundary marked by arrows. (*Continued*.)

(c)

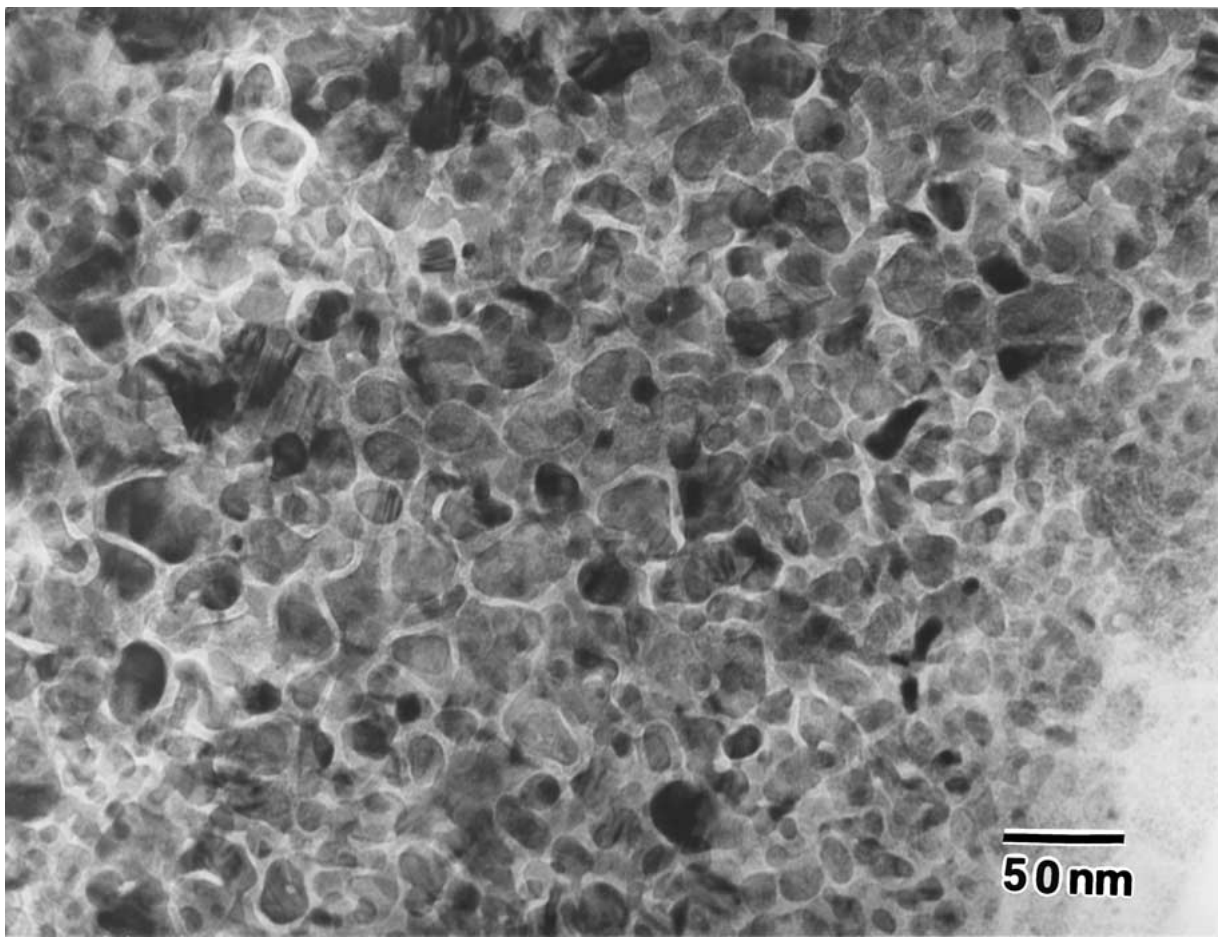

(d)

Figure 4 (*Continued*.)

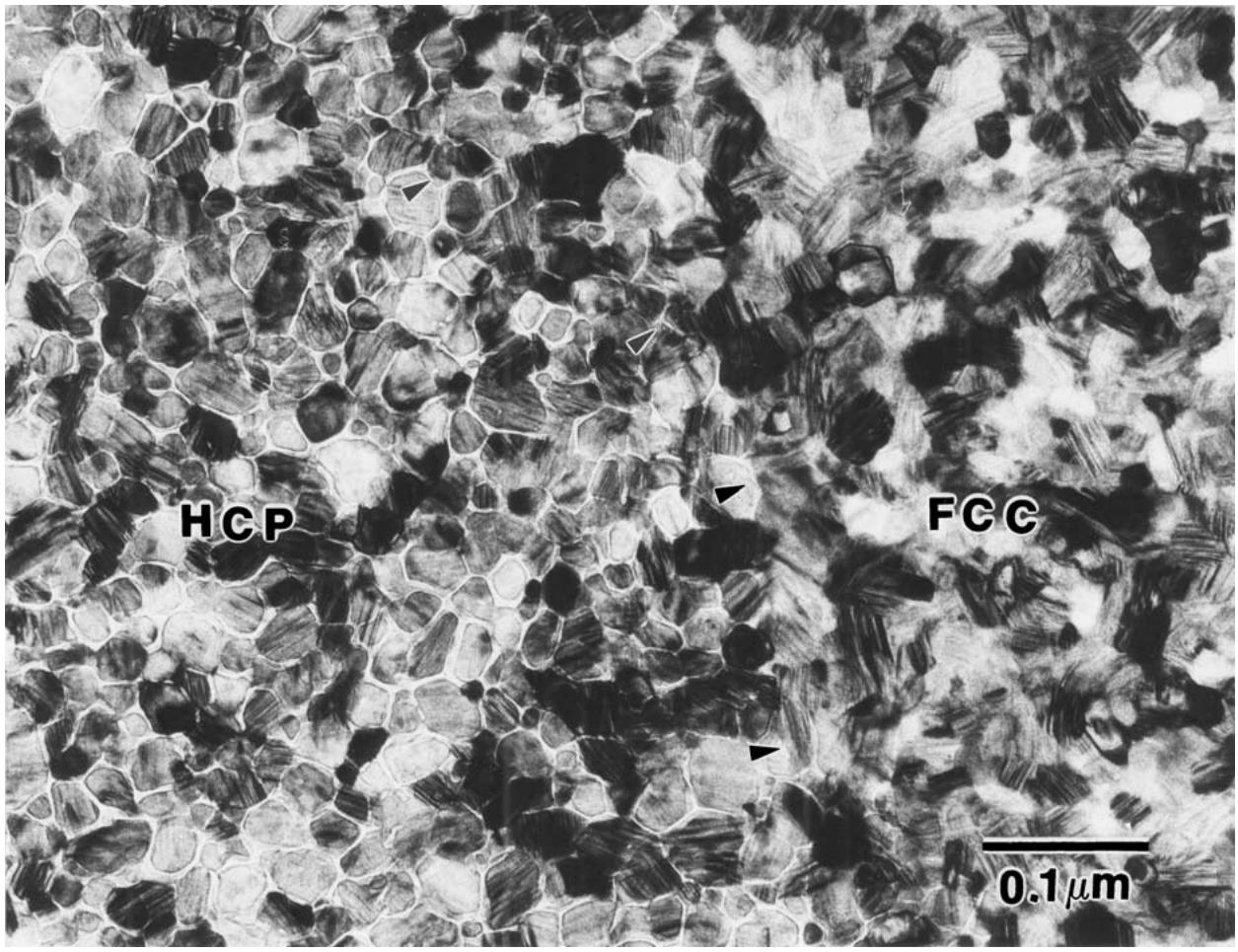

(e)

Figure 4 (*Continued*.)

In the intermediate region, the crystallized sub-layer was sensitive to the annealing temperature. Below 400°C, the HCP crystals with the oxygen fault started to nucleate and grow. As the annealing temperature increased, FCC structure was favored. In the two-phase region, as can be seen in Fig. 4e, the oxygen fault developed on the FCC phase while the HCP phase was free from the fault, which is reasonable since the oxygen condensation appear to occur preferentially on FCC {111} planes as seen in the low temperature region of the boron-rich composition. Above the two-phase region, the high temperature form of crystalline Co structure was found while the oxygen fault was annealed out.

4. Conclusion

The non-equilibrium crystallization diagram for the Co sub-surface layer of for the $Co_{75.26-x}Fe_{4.74}(BSi)_{20+x}$ amorphous alloy for $x > 1$ during magnetic field annealing is determined using TEM. The diagram shows that, depending on the composition and the temperature, the Co sub-layer exhibits five distinctively different microstructures which are strongly correlated to the magnetic properties of the amorphous alloy. Such a map provides a guide to designing and optimizing the composition and processing conditions to obtaining desired properties of the amorphous alloy.

References

1. F. E. LUBORSKY, in "Amorphous Magnetism II," edited by R. A. Levy and R. Hasegawa (Plenum Press, New York, 1977) p. 345.
2. S. CHIKAZUMI, in "Physics of Magnetism," edited by S. Chikazumi and S. H. Charap (John Wiley & Sons, New York, 1965) p. 497.
3. C. K. KIM and R. C. O'HANDLEY *Metal. Mat. Trans. A* **28A** (1997) 423.
4. C. K. KIM, *Mat. Sci. Eng.* **B38** (1996) 194.
5. *Idem*., *ibid.* **B40** (1996) 10–18.
6. R. W. G. WYCKOFF, "Crystal Structures" (John Wiley & Sons, New York, 1963) p. 10.
7. C. K. KIM and R. C. O'HANDLEY, *J. Microscopy* **180** (1995) 70.
8. S. C. BYEON, C. K. KIM, K. S. HONG and R. C. O'HANDLEY, *Mat. Sci. Eng.* **B60**(1) (1999) 58.
9. H. FUJIMORI, in "Amorphous Alloys," edited by F. E. Luborsky (Buttersworth, London, 1983) p. 300.
10. H. R. HILZINGER and G. HERZER, *Mat. Sci. Eng.* **B99** (1988) 101.
11. G. HERZER, *Physica Scripta* **T49A** (1993) 307.
12. C. K. KIM, C. S. YOON, T. Y. BYUN and K. S. HONG, *Oxidation of Metals*, accepted.

Received 6 November 2000
and accepted 6 June 2001